Chinese Chemical Letters 34 (2023) 108128

Contents lists available at ScienceDirect

Chinese Chemical Letters

journal homepage: www.elsevier.com/locate/cclet

Morphological and heterojunctional engineering of two-dimensional porous Mo-Ni based catalysts for highly effective catalytic reduction of aromatic nitro compounds

Zexu Fang[a], Ying Gu[a,*], Xinran Dong[a], Gen Zhang[a], Lin Li[a], Xiaoguang Zhou[a,*], Chungui Tian[b,*]

[a] College of Chemistry, Chemical Engineering and Resource Utilization, Northeast Forestry University, Harbin 150040, China
[b] Key Laboratory of Functional Inorganic Material Chemistry, Ministry of Education of the People's Republic of China, Heilongjiang University, Harbin 150080, China

ARTICLE INFO

Article history:
Received 8 November 2022
Revised 6 December 2022
Accepted 30 December 2022
Available online 4 January 2023

Keywords:
Hydrogenation
Nitro compounds
Two-dimensional sheets
Heterojunction
Nitrides

ABSTRACT

Hydrogenation reactions play crucial roles on chemical synthesis and pollutant elimination. The improvement of the ability to activate reactants and increase of the contact probability between the catalysts and reactants are positive to improve the catalytic performance. Herein, we have reported the design of two-dimensional porous Ni-Ni_3N-NiMoN heterojunction sheets (2D Mo-Ni based nanosheets) for efficient catalytic hydrogenation of the aromatic nitro-compounds. The heterojunction interfaces provide plentiful active sites to improve the activating ability of the catalyst on the reactants. Additionally, the 2D porous structure facilitates not only the contact of catalytic sites with reactants but also mass transfer and diffusion, both of which are favorable to accelerating the hydrogenation process. As a result, the optimized sample of 2D Mo-Ni sheet exhibits good activity for the hydrogenation of aromatic nitro-compounds by converting 0.2 mmol/L (30 mL) of *p*-nitrophenol to *p*-aminophenol within 45 s with good recyclability. The activation energy and the reaction rate at 25 °C is 31.11 kJ/mol and 0.0796 s^{-1}, respectively, both of which surpass most of reported non-noble metal catalysts and rivals with most noble metal-based catalysts. The combination of late and early transition metals provides an innovative way to obtain outstanding catalysts for the hydrogenation.

© 2023 Published by Elsevier B.V. on behalf of Chinese Chemical Society and Institute of Materia Medica, Chinese Academy of Medical Sciences.

Though the technological and industrial development brings many positive effects, it also accompanies unprecedented damage to the environment [1–3]. Therefore, it is necessary and urgent to exploit efficient strategy to reduce the environmental damage or to take remedial actions for sustainable development [4–6]. The hydrogenation reactions are important processes for the synthesis of chemicals and elimination of environmental pollution [7,8]. As known, some chemicals with -NO_2 groups are main raw materials for the synthesis of dyes and other chemicals [9,10]. However, these chemicals are chemically stable, hardly degradable, and strongly toxic, being potentially dangerous to human and aquatic organisms [11,12]. Therefore, it is a great demand to converse or eliminate aromatic nitro-compounds for the sustainable development [13,14]. Among the existing researches, converting environment-polluting nitrophenol into highly medicinal-value aminophenol (hydrogenation of nitrophenol) is proved to be an efficient methodology [15,16]. Besides, the conversion reaction (hydrogenation of *p*-nitrophenol) is also an important model for evaluating the potential ability of catalysts in hydrogenation reactions [17–19]. Therefore, the design of effective catalysts is the key to promoting the reaction, due to the high energy barrier of the reaction under the normal condition.

Noble metals (Pt, Pd) are state-of-the-art catalysts for the hydrogenation reaction due to the strong ability to release active H species due to the unique and proper electronic configuration [20,21]. However, the expensive and rare characterization limit the wide use of the noble metal-based catalysts [22,23]. Remarkably, the Ni element is a promising candidate to replace the noble metals Pt and Pd, because Ni locates the same group as Pt and Pd, but much cheaper than them. Moreover, the valence electron d orbits of Ni are considered as the catalytic activity center according to the d-band center theory [24–27]. However, the single-component Ni catalysts exhibit unsatisfactory performance for hydrogenation

* Corresponding authors.
E-mail addresses: guying@nefu.edu.cn (Y. Gu), zhouxg78@nefu.edu.cn (X. Zhou), tianchungui@hlju.edu.cn (C. Tian).

https://doi.org/10.1016/j.cclet.2022.108128
1001-8417/© 2023 Published by Elsevier B.V. on behalf of Chinese Chemical Society and Institute of Materia Medica, Chinese Academy of Medical Sciences.

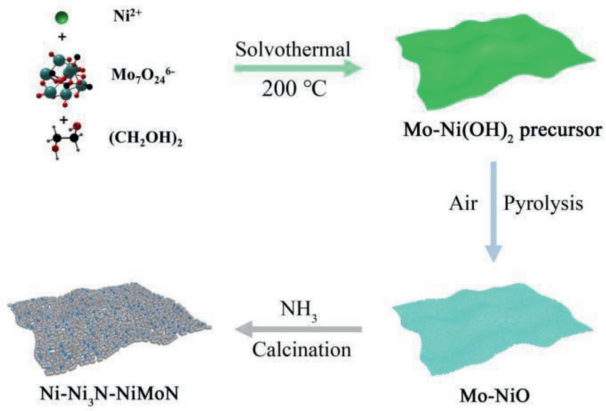

Scheme 1. Schematic illustration of the preparation of 2D porous Ni-Ni_3N-NiMoN heterojunction nanosheets.

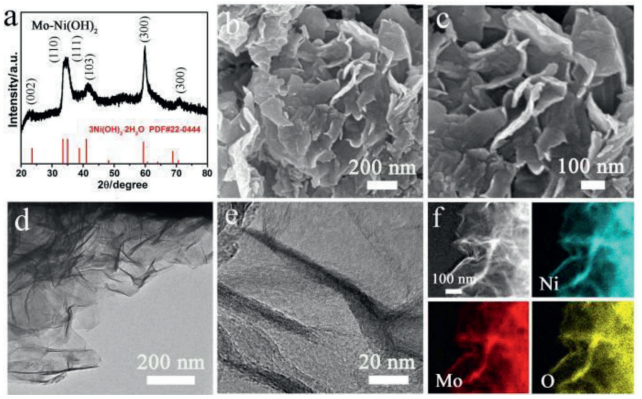

Fig. 1. (a) XRD pattern, (b, c) typical SEM images, (d, e) TEM images, (f) STEM and corresponding EDS elemental mapping images of Mo-modified 2D $Ni(OH)_2$ precursor.

of *p*-nitrophenol [28]. This results from that the two unpaired electrons in the d orbital of Ni ($3d^84s^2$), which is different from that of Pt ($5d^96s^1$) [29–32]. To address this disadvantage, a series of strategy have been developed to tune the electron structure by the construction of the heterojunction, alloying (Ni-Pt, Ni-Cu, Ni-Mo) and modification, thereby enhancing the intrinsic activity [33–35]. Especially, a combination of Ni with Mo components can give optimized electronic structure similar to Pt. For instance, Duan *et al.* have synthesized 2D nickel-molybdenum nanosheets with tetragonal $MoNi_4$ phase for efficient catalytic cracking of HOR in alkaline electrolytes [36]. Our group have also reported the electronic tuning between Ni and Mo species anchored on SAPO-11 (Ni-Mo/S-11) for the hydroisomerization of *n*-alkanes with performance close to the commercial Pt/S-11 [37]. However, the rational combination of Ni and Mo for the hydrogenation of *p*-nitrophenol reaction has not yet been studied.

Here, we have reported the design of two-dimensional porous Ni-Ni_3N-NiMoN heterojunction sheets (2D Mo-Ni-based nanosheets). The construction of heterostructures was benefit for modulating the surface electronic structure, inducing synergistic effect among different components, and expose more active sites. Therefore, the charge density around Ni-components was increased, being closer to that of Pt by the electrons transfer from Mo to Ni component. Thus, the activation ability of Ni to the reactants can be improved [38,39]. Based on this, the 2D Ni-Ni_3N-NiMoN heterojunction sheets were utilized to evaluate the performance of the hydrogenation of aromatic nitro-compounds. The relating mechanism has also been systematically investigated. The study would be promising to design outstanding catalysts for hydrogenation by rationally combining late and early transition metals.

It is difficult to directly synthesize the metallic Ni-based 2D sheets. Fortunately, the $Ni(OH)_2$, which is a suitable precursor toward Ni-based materials, can be facilely synthesized with 2D morphology. So, the 2D Mo-modified $Ni(OH)_2$ precursors were firstly synthesized through solvothermal reaction of $Ni(NO_3)_2{\cdot}6H_2O$ and $(NH_4)_6Mo_7O_{24}{\cdot}4H_2O$ in an $NH_3{\cdot}H_2O$/ethylene glycol/H_2O mixture solution. Then, the precursor was calcined in a muffle furnace and then reduced in a tube furnace under an NH_3 atmosphere, thereby obtaining the Ni-Ni_3N-MoNiN nanosheets (Scheme 1 and Table S1 in Supporting information). The X-ray diffraction (XRD) pattern (Fig. 1a) of the precursor showed four peaks located at 33.67°, 35.20°, 41.20° and 59.60°, assigned to the (110), (111), (103) and (300) planes of $Ni(OH)_2{\cdot}2H_2O$ (JCPDS No. 22-0444), respectively. The peaks corresponding to the Mo species were indiscernible, ascribing to the low amount of Mo during the synthesis. The scanning electron microscopy (SEM) image clearly showed the formation of 2D thin sheets with obvious stacking (Fig. 1b). A magnifying image in Fig. 1c revealed a less than 10 nm thichness for the prepared sheets. Furthermore, the transmission electron microscopy (TEM) image showed that the precursor was large-scaled sheets with curved surface (Fig. 1d) [40]. From the high-resolution TEM image in Fig. 1e, we can observe many "black wires" which should be folded edge of the sheets. From this, the thickness of the sheets was estimated to be below 10 nm, which was consistent with that of SEM images. In addition, the STEM images further showed the formation of thin 2D sheets. The Energy dispersive spectroscopy (EDS) mapping (Fig. 1f) demonstrated the uniform distribution of the Mo, Ni, and O elements throughout the sheets. The atom ratio of Mo from quantitative analysis of EDS was about 10.93% which is close to the atomic ratio of Ni-Mo shown by inductively coupled plasma (ICP), and also consistent with the theoretical ratio of feeding during the synthesis process (Fig. S1 and Table S2 in Supporting information). The presence of Mo verified the formation of Mo-modified 2D $Ni(OH)_2$ sheets. In the synthesis process, the ratio of ammonium molybdate to nickel nitrate was the key to the formation of sheet precursors. The precursors synthesized without ammonium molybdate or with a small amount of ammonium molybdate were irregular sheet structures (Figs. S2 and S3 in Supporting information). The precursors synthesized without $Ni(NO_3)_2{\cdot}6H_2O$ was an irregular sphere (Fig. S4 in Supporting information). When the molar ratio of ammonium molybdate to nickel nitrate was 1:50, the precursor obtained is a regular thin 2D sheets structure. When the molar ratio of ammonium molybdate to nickel nitrate was 1:10, the precursor was block-structure (Fig. S5 in Supporting information). Therefore, the appropriate ratio of ammonium molybdate to nickel nitrate was very important for the preparation of regular thin sheet precursors.

Based on our previous studies, the oxides were easier to be reduced by NH_3 to form corresponding metals or nitrides. Therefore, the Mo-modified $Ni(OH)_2$ precursor was first calcined in a muffle furnace at a low temperature to convert into corresponding oxides. After the operation, the $Ni(OH)_2$ can be converted into the NiO by the loss of H_2O, and the Mo-modified 2D $Ni(OH)_2$ precursor was transformed into Mo-modified 2D NiO. The color of solid powders changed from original green to yellow, indicating the formation of the oxides. The XRD pattern of the sample showed the broad diffraction peaks at 37.25°, 43.30° and 62.90°, ascribing to (101), (012) and (104) planes of the NiO phase (JCPDS No. 44-1159) (Fig. 2a), implying the conversion of $Ni(OH)_2$ to NiO by pyrolysis. Similar to the case of the precursor, there was no diffraction peak of Mo-related species, ascribing to the low amount of Mo and their modification on NiO. In addition, the position of all three diffrac-

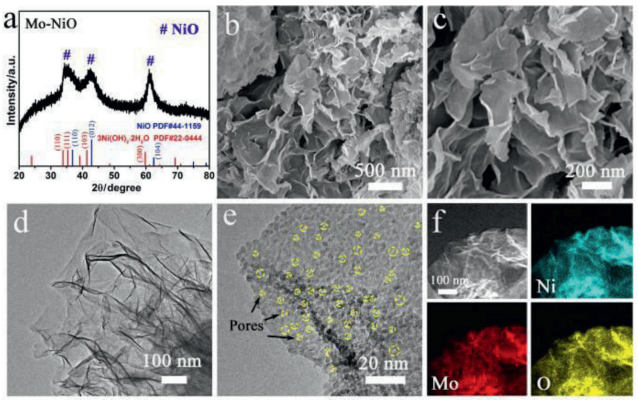

Fig. 2. (a) XRD pattern, (b, c) typical SEM images, (d, e) TEM images, (f) STEM and corresponding EDS elemental mapping images of Mo-NiO.

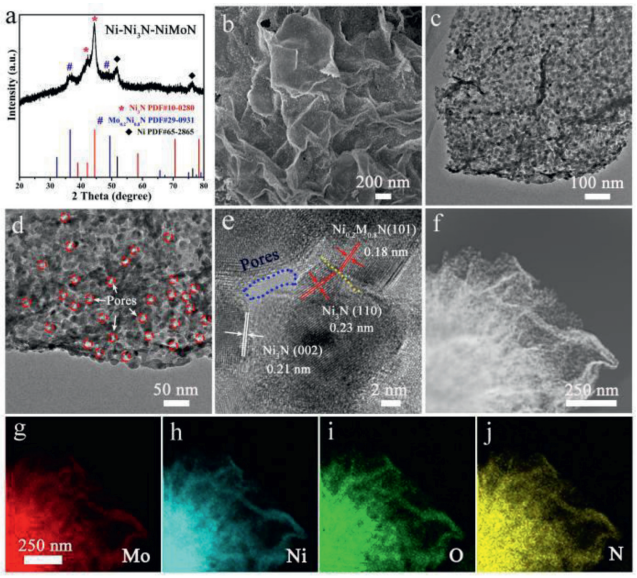

Fig. 3. (a) XRD pattern, (b) typical SEM images, (c–e) TEM images, (f–j) STEM and corresponding EDS elemental mapping images of Ni-Ni_3N-NiMoN.

tion peaks of Mo-NiO slightly shifts to lower angles in comparison with that shown in the standard card. The result can be ascribed to the doping Mo in NiO crystal lattice. The morphology of 2D Mo-modified NiO was further studied by SEM and TEM images. The SEM image showed the presence of sheets with raised edges, agreeable with the precursor both in the morphology and thickness (Figs. 2b and c). The TEM images (Fig. 2d) further showed that the morphology of Mo-modified NiO was similar to the precursor with folded thin-sheet structure (Fig. 1d). However, the enlarged image (Fig. 2e) shows that the sheets were composed of many particles with sizes of about 3 nm, being obviously different from the precursor sheets (Fig. 1e). Also, there are many pores between the particles, which is favorable for the mass transfer and diffusion during the reaction. The formation of pores and particles should be related with the decomposition and release of H_2O during the calcination. The STEM images showed the maintenance of the sheet-like structure after calcination in the air atmosphere. The EDS mapping (Fig. 2f) indicated that Mo, Ni, and O elements were uniformly distributed throughout the sheets. The atomic percentage of Mo was about 3.34% based on the quantitative analysis of EDS (Fig. S6 in Supporting information) and the molar ratio of Ni:Mo was approximate 6.25:1 (Table S3 in Supporting information). The result indicated the successful formation of 2D Mo-modified NiO which can be used for the synthesis of Ni-based catalysts.

As known, the NH_3 can act as N source and reduction agent during the synthesis, being helpful to form Ni-based catalysts. Followed the calcination under air, the 2D Mo-modified NiO was further treated under NH_3 atmosphere. The resulting product was detected by XRD to disclose the phase components in Fig. 3a. The intensive diffraction peaks located at 38.94°, 42.11° and 44.48° coincided well with (110), (002) and (111) planes of Ni_3N (JCPDS No. 10-0280). The diffraction peaks at 44.50°, 51.85° and 76.38° arised from (111), (200), and (220) planes of metallic Ni (JCPDS No. 65-2865). It was noteworthy that the low intensity peaks correspond to $Ni_{0.2}Mo_{0.8}N$ (JCPDS No. 29–0931) indicated the successful formation of Ni-Ni_3N-NiMoN compound. The SEM and TEM were used to further study the morphology of Ni-Ni_3N-NiMoN sample. The SEM image (Fig. 3b) illustrated the as-prepared Ni-Ni_3N-NiMoN sample inherited the thin sheets morphology of the original Mo-$Ni(OH)_2$ precursor. Moreover, unlike the Mo-$Ni(OH)_2$ and Mo-NiO samples with smooth surfaces, many “bright dots” can be observed on the Ni-Ni_3N-NiMoN sheets. The observation was related to the formation of small Ni particles. The emergency “bright dots” was ascribed to the good conductivity of the metallic Ni. The TEM (Fig. 3c) image gave the direct observation of the formation of 2D sheets composed of small particles. As shown in Fig. S7 (Supporting information), the average particle size is 19.6 nm for Ni-Ni_3N-NiMoN catalysts. It can be seen that the thickness of nanosheet is less than 10 nm based on the folds of the edge. The size of particles and pores was slightly larger than that composed of 2D Mo-NiO sheets, which was related to the quick decomposition of Mo-modified NiO under reduction conditions accompanied with a slight particles agglomeration (Fig. 3d). As shown in Fig. S8 (Supporting information), the N_2 adsorption-desorption test shows that the Ni-Ni_3N-NiMoN heterostructure catalysts exhibit well-developed porous structure (adsorption average pore diameter: 13.9 nm) with a Brunauer-Emmett-Teller (BET) surface area of 162 m^2/g. The porous structure was beneficial to the diffusion of reactants and provides more access to inner reactive site during the catalysis process. The high-resolution TEM (HRTEM) image showed the two ordered lattice fringes with distances of 0.21 nm and 0.18 nm, which corresponded to the (111) and (101) crystal planes of Ni_3N and NiMoN (Fig. 3e). Notably, the contact between two adjacent particles can be observed in the HRTEM image, indicating the formation of intimately contacted heterointerfaces [41]. As shown in the HRTEM image (Fig. 3e), the heterojunction consists of two different components. The $Ni_{0.2}Mo_{0.8}N$ and Ni_3N nanoparticles are interweaved with each other which provide the formation of intimately contacted heterointerfaces. The close contacted heterogeneous surface can promote electron transfer, influence the adsorption/desorption energies of active species in catalytic reactions, and thus regulate catalytic ability in the reductive hydrogenation reaction. In addition, the TEM images showed the presence of pores. These open spaces were expected to create more accessible active sites and provide multiple pathways for fast mass and electron transport, in favor of the solution-phase catalysis. The STEM image and corresponding to the EDS mapping indicated that Mo, Ni, O and N elements were uniformly distributed throughout the sheets (Figs. 3f–j). Based on the quantitative analysis of EDS, the atomic percentage of Mo was about 10.27% and the Ni-Mo ratio displayed by ICP was about 6.33 (Fig. S9 and Table S4 in Supporting information). Above tests showed the successful construction of 2D porous Ni-Ni_3N-NiMoN heterostructure nanosheets. For comparison, the pure Mo-base precursor and pure Ni-base precursor were also pyrolyzed in two-step pyrolysis. The XRD and SEM results in Fig. S10 (Supporting information) showed that Ni catalyst and MoO_2 catalyst with irregular morphology were obtained

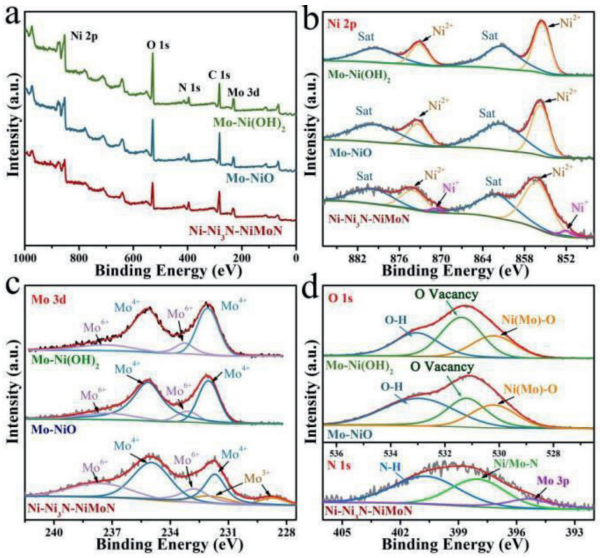

Fig. 4. XPS spectra of the Mo-Ni(OH)$_2$ precursors, Mo-NiO, and Ni-Ni$_3$N-NiMoN: (a) Wide scan spectrum and the high-resolution spectra of (b) Ni 2p, (c) Mo 3d, (d) O 1s and N 1s-Mo 3p.

after pyrolysis, respectively. It showed that the interaction between Mo and Ni was favorable for the formation of nitrides. The influence of pyrolysis temperature on the structure and morphology of the catalyst was studied by adjusting the calcination temperature of the catalyst under NH_3 atmosphere. From the XRD and SEM results of samples calcined at different temperatures, it can be seen that NiO is difficult to be reduced when the pyrolysis temperature is low (375 °C) (Fig. S11 in Supporting information). When the pyrolysis temperature rase to 450 °C, the nanoparticles forming the 2D sheets appear agglomeration, and the particles became larger obviously. (Fig. S12 in Supporting information).

The elemental composition and valence states of the Mo-Ni(OH)$_2$ precursors, Mo-NiO, and Ni-Ni$_3$N-NiMoN were further investigated by X-ray photoelectron spectroscopy (XPS). The survey spectra of samples (Fig. 4a) confirmed the existence of all the elements including Ni, Mo, N and O. In the high-resolution Ni 2p spectra (Fig. 4b), for Mo-Ni(OH)$_2$ precursors and Mo-NiO, the doublet peaks at 855.6 and 873.2 eV represented the characteristic Ni 2p$_{3/2}$ and Ni 2p$_{1/2}$ of divalent Ni from NiO with doublet satellites at 879.6 and 861.5 eV, respectively [42,43]. For the 2D Ni-Ni$_3$N-NiMoN sample, the peaks at 871.0 and 852.1 eV were ascribed to Ni-N from Ni$_3$N, which was consistent with XRD results. Meanwhile, the peaks located at 880.2 and 862.2 eV were ascribed to Ni satellite peaks.

The Mo 3d spectrum (Fig. 4c) of Mo-Ni(OH)$_2$ precursors and Mo-NiO sample showed four peaks at 232.1 and 235.2 eV, 233.2 eV and 237.2 eV, which can be attributed to Mo^{4+} and Mo^{6+}, respectively, corresponding to oxidized Mo species (Mo-O bond) [44,45]. For the 2D Ni-Ni$_3$N-NiMoN sample, the fitting revealed three oxidation states (+3, +4 and +6) for Mo on the surface of NiMoN, the Mo^{3+} is from the Mo-N bonds in NiMoN, while Mo^{4+} and Mo^{6+} species were attributed to the surface oxidization of Ni-Ni$_3$N-NiMoN upon air exposure. In the O 1s XPS spectra shown in Fig. 4d, the peak centered at 533.0 eV corresponded to the O–H bond arising from the adsorbed H_2O, while the two other peaks at 531.2 and 530.2 eV can be assigned to the lattice oxygen of O-M (M = Ni, Mo) bond and oxygen vacancies. It is clearly seen from the XPS spectra of N 1s for Ni-Ni$_3$N-NiMoN sample that N 1s and Mo 3p have partial overlap. The peak located at 395.3 eV corresponded to Mo 3p$_{3/2}$. The peak at 398.1 can be assigned to Ni/Mo-N in Ni$_3$N/NiMoN, which further indicated the formation of the nitride. Other N 1s peak at 400.8 eV can be ascribed to N–H groups, which suggested that there are abundant H species at the surface of the catalysts. This result indicated that N ions at the surface were able to strongly interact with H species, and a large number of N–H moieties should be available to participate in the reduction of aromatic nitro compounds.

The 4-nitrophenol (4-NP), which was listed as a priority pollutant by the US Environmental Protection Agency, had carcinogenicity and genotoxicity to humans and wild animals, and can lead to many diseases like methemoglobinemia [46,47]. However, the reduction product aromatic amines were important intermediates for the manufacturing of various fine chemicals and has lower toxicity than 4-NP [48–50]. Thus, the reduction of 4-NP into 4-AP with $NaBH_4$ was used as a model catalytic reaction to evaluate the catalytic performance of the 2D Ni-Ni$_3$N-NiMoN heterojunction sheets catalyst for demonstrating their structural advantage in the catalysis [51–53]. The 4-NP reduction reaction progress process was monitored by the UV-vis spectrometer. As shown in Fig. 5a, the *p*-nitrophenolate anion solution exhibits a strong absorption peak at 317 nm. After the addition of $NaBH_4$, the absorption peak occurred a red-shifted to 400 nm, accompaning with the color of the solution changing from light yellow to bright yellow because of the formation of *p*-nitrophenolate anion. Notably, the maximum absorption of the solution can remain for more than 30 min in the absence of any catalysts, indicating that the addition of $NaBH_4$ alone will not trigger 4-NP reduction reaction. Fig. 5b showed the time-dependent absorption spectra of solution over 2D Ni-Ni$_3$N-NiMoN sheets catalyst in the presence of excess $NaBH_4$. It can be seen from the photo in Fig. 5b that the dispersion of the catalyst had the Tyndall effect, indicating the colloidal dispersity in an aqueous solution, which was conducive to the exertion of the catalytic activity of the catalyst. The maximum absorbance peak at 400 nm gradually declined as the reduction reaction time proceeds, while a new absorption peak attributed to 4-aminophenol ions began to rise as a shoulder at 295 nm. The yellow color of the 4-NP solution discharged in 45 s under continuous stirring signaling the completion of conversion of 4-NP to 4-AP. However, it took 48 min for Mo-NiO catalyst to completely convert 4-NP to 4-AP, indicating that the formed nitrides were beneficial to the catalytic performance of the catalyst (Fig. 5c). The thermodynamic parameters for the reduction of 4-NP were subsequently investigated by performing the reaction at different temperatures (15, 25, 35 and 45 °C) (Fig. 5d and Fig. S13 in Supporting information). Since the concentration of $NaBH_4$ can be considered as a constant because it is in great excess, the reaction rate was controlled by the adsorption of 4-nitrophenol on catalysts, following the pseudo-first-order kinetics [54,55]. The plot of logarithm of absorption versus reaction time can be fitted linearly. The slope, *i.e.*, apparent rate constant values (k), was found to be 0.0722, 0.0796, 0.1396 and 0.2149 s^{-1} for the reactions in 15, 25, 35 and 45 °C, respectively (Fig. 5e). In general, the reaction rate increases with the increase of temperature. The apparent activation energy (E_a) was estimated with the Arrhenius equations (Eq. 1) [56,57]:

$$\ln k_{app} = \ln A - \frac{E_a}{RT} \quad (1)$$

where k_{app} and R are the reaction rate constant and the molar gas constant (8.314 J K^{-1} mol^{-1}) at the reaction temperature T. E_a and A are the apparent activation energy and pre-exponential factor. The activation energy shows the effect of temperature on the catalytic performance.

From the plot of ln(k_{app}) *versus* 1000/T, the activation energy was obtained to be 31.11 kJ/mol, which indicated that the reduction of 4-NP in the 2D Ni-Ni$_3$N-NiMoN sheets catalytic system meets the surface catalyzed reaction process. As shown in Fig. S14 (Supporting information), the pure Ni and MoO_2 catalysts required 10

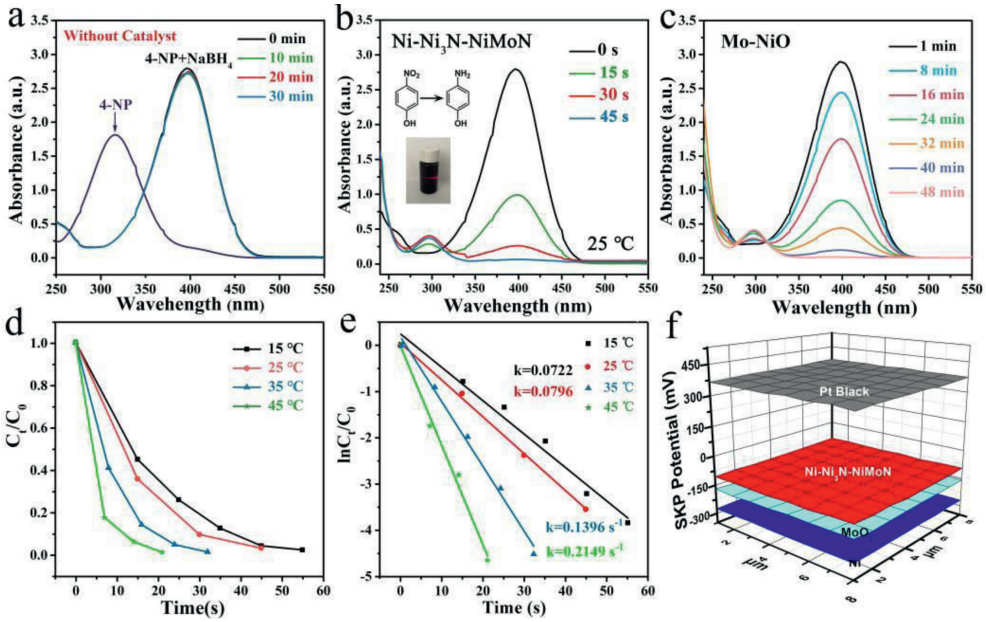

Fig. 5. (a) The UV-vis absorption spectra of 4-NP solution with and without $NaBH_4$. (b) Change in the absorbance of solution at 400 nm in the presence of $NaBH_4$. (c) UV-vis absorbance spectra for the reduction of 4-NP in the presence of the Mo-NiO catalyst; Plots of (d) C_t/C_0 and (e) $\ln(C_t/C_0)$ *vs.* time at different temperature. (f) Work function comparison of Pt black, Ni-Ni_3N-NiMoN, MoO_2 and Ni.

and 180 min to completely convert 4-NP to 4-AP, respectively, indicating that the interaction between Mo components and Ni components was beneficial to the catalytic performance. In order to study the influence of the presence of metallic Ni generated during pyrolysis on the catalytic activity of the catalyst, we soaked the catalyst with 1 mol/L HCl solution to remove metallic Ni. Fig. S15 (Supporting information) shows that it takes 180 s for Ni-Ni_3N-NiMoN catalysts to convert 0.2 mmol/L (30 mL) of *p*-nitrophenol to *p*-aminophenol, indicating that the presence of metallic Ni is beneficial to the catalytic activity of the catalyst. In addition, the work functions (WF) of Pt, pure-Ni, MoO_2 and Ni-Ni_3N-NiMoN samples were also measured to evaluate the electron capture ability by using scanning Kelvin probe (SKP) technology (Fig. 5f). The work function values of Pt, Ni, MoO_2 and Ni-Ni_3N-NiMoN were 5.65, 5.07, 5.17 and 5.24 eV, respectively. The WF value of Ni-Ni_3N-NiMoN is close to that of Pt/C catalyst, indicating its strong ability to capture electrons, being favorable to enhance the catalytic hydrogenation activity.

In addition, the pyrolysis temperature (NH_3) during the preparation of the catalyst also affects the catalytic activity of the catalyst. As shown in Fig. 6a, it took a long time (80 min) for the Mo-Ni-375 catalyst to reduce 4-NP to 4-AP, which was consistent with XRD results that NiO was difficult to be reduced at low pyrolysis temperature. When the pyrolysis temperature rises to 450 °C, the nanoparticles composed of the sheet material were obviously agglomerated, so that the catalytic activity of the catalyst was significantly reduced (Fig. 6b). The slope, *i.e.*, apparent rate constant values (k), was found to be 0.0001, 0.0796, and 0.0623 s^{-1} for the reactions using Mo-Ni-375, Ni-Ni_3N-NiMoN, and Mo-Ni-450 catalysts, respectively (Figs. 6c and d). The recyclability of catalyst was a very important parameter to evaluate a heterogeneous catalytic process. Fortunately, the magnetism of as-prepared 2D Ni-Ni_3N-NiMoN sheets catalyst was expected to allow easy separation from aqueous reaction media, thus allowing facile catalyst reuse (Fig. 6e). The 2D Ni-Ni_3N-NiMoN heterojunction catalyst were able to be recycled and reused over at least 10 successive cycles of catalytic reduction, with high 4-NP reduction efficiencies (90%) achieved within 40 s during each reuse cycle implying the good stability of the catalyst (Fig. 6f). Also, the hot filtration test show that the conversion cannot be happened with no assistance of Ni-Ni_3N-NiMoN, further indicating the excellent stability and heterogeneous characteristics of Ni-Ni_3N-NiMoN catalyst. (Fig. S17 in Supporting information). As shown in Fig. S16 (Supporting information), the diffraction peaks of the sample after catalytic hydrogenation of 4-NP was similar to that of the original Ni-Ni_3N-NiMoN catalysts, implying the good stability of the catalyst. Impressively, compared to the previously reported noble metal-based nanomaterials, the 2D Ni-Ni_3N-NiMoN heterojunction catalysts showed comparable or even better catalytic activity (Fig. 6g and Table S5 in Supporting information). In order to better compare the catalytic efficiency of the Ni-Ni_3N-NiMoN heterojunction catalyst prepared in this paper with other materials, the Turn over frequency (TOF) value defined as the molar amount of 4-NP that 1 mol active metal site of a catalyst can convert into 4-AP per unit time for the Ni-Ni_3N-NiMoN was calculated to be 0.136 mmol mg^{-1} min^{-1}, which is comparable or higher than some precious metal-based catalysts and non-precious metal-based catalysts (Table S6 in Supporting information).

Besides 4-NP, many aromatic amines are important intermediates in the preparation of several nitrogen-containing biologically active compounds, agrochemicals, pharmaceuticals, *etc.* Therefore, it is particularly important to prepare non-noble metal catalysts with high efficiency for the reduction of various aromatic nitro compounds. As shown in Fig. S18 (Supporting information), Ni-Ni_3N-NN-NiMoN catalysts only needed 20 and 30 s to reduce *o*-nitrophenol and *m*-nitrophenol to form corresponding aminobenzene. Some complex nitrobenzene containing more functional groups can also be reduced to corresponding aminobenzene within a short time (Fig. S19 in Supporting information). Therefore, the prepared porous Ni-Ni_3N-NiMoN sheets catalysts have excellent catalytic hydrogenation activity for many aromatic compounds, which was beneficial to their practical application.

A possible catalytic mechanism for the reduction of 4-NP by Ni-Ni_3N-NiMoN sheets catalyst has also been proposed in Fig. 7 based on the experimental results mentioned above. The catalytic reduction process followed Lambert Beer's law [58], in where the reactants (4-NP and BH_4^-) were adsorbed on the catalyst surface and electrons/protons are transferred through the catalyst. Firstly, BH_4^-

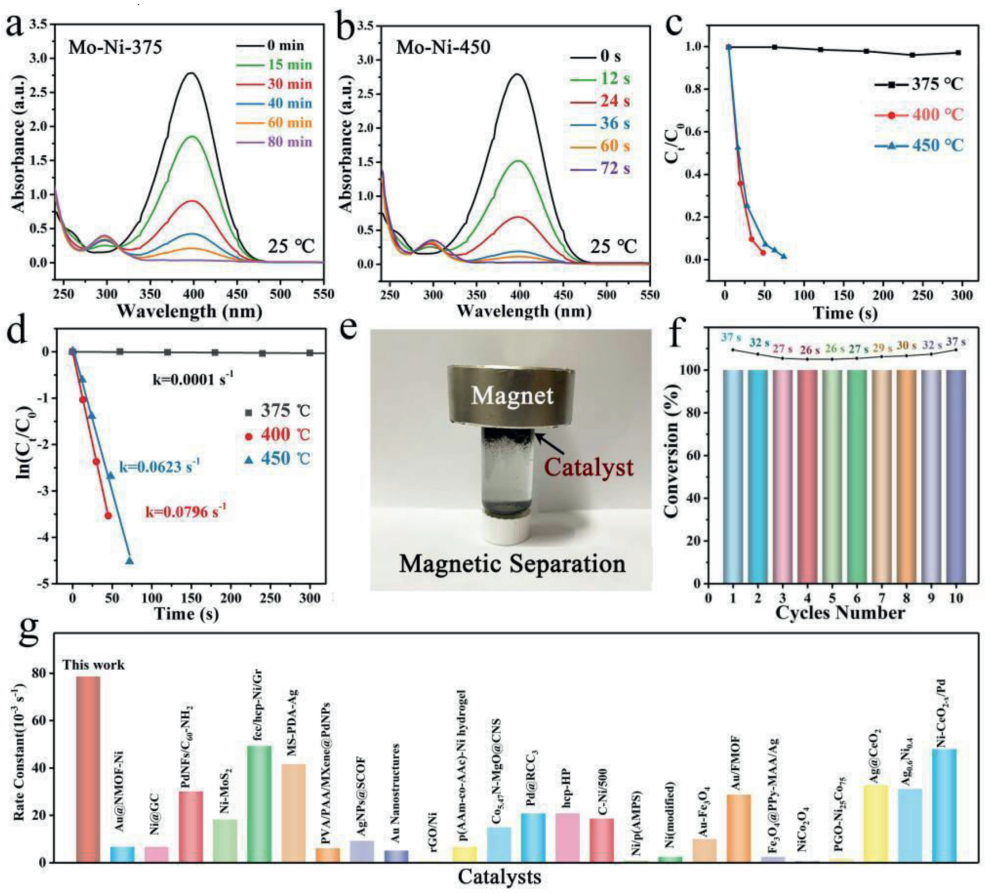

Fig. 6. UV-vis absorption spectra of 4-NP solution at different contact time with (a) Mo-Ni-375 and (b) Mo-Ni-450. Plots of (c) C_t/C_0 and (d) $\ln(C_t/C_0)$ against contact time for the reduction of 4-NP reactions catalyzed by Mo-Ni-375, Ni-Ni_3N-NiMoN (Mo-Ni-400) and Mo-Ni-450. (e) The magnetic property of Ni-Ni_3N-NiMoN. (f) The reusability of Ni-Ni_3N-NiMoN. (g) The comparison of catalytic performance of Ni-Ni_3N-NiMoN with recently reported catalysts.

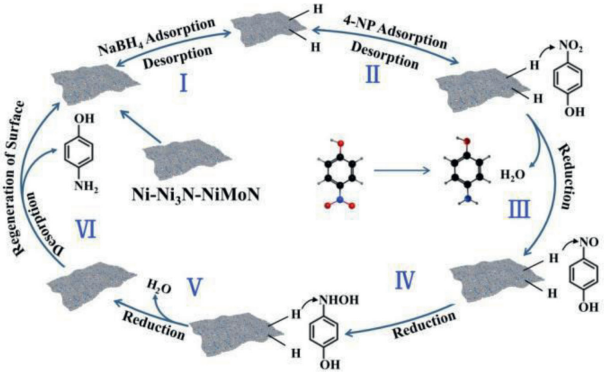

Fig. 7. Proposed mechanism for the hydrogenation of 4-NP over Ni-Ni_3N-NiMoN nanosheets.

ions reacted with H_2O to produce BO_2^- and H in the aqueous solution and the produced H instantly combined with 2D Ni-Ni_3N-NiMoN catalyst to formed metal-H species [59,60]. Meanwhile, the 4-NP molecules were also transferred and reversibly absorbed on the 2D Ni-Ni_3N-NiMoN catalyst. Then the surface-hydrogen species and electron transferred to the 4-NP, which went through several steps of hydro deoxygenation reactions to yield the final product, 4-AP [61,62]. The free 4-AP molecules were desorbed from the catalyst surface and released into the reaction solution, while the catalysts returned to initial state for the next catalytic cycle [63,64]. By combining a series of experimental and characterization results, the good catalytic activity of 2D Ni-Ni_3N-NiMoN sheets catalyst for the hydrogenation of nitro compounds was comparable to that of noble metal-based catalysts. The possible reason was that the electrons transfer from the Mo component to the Ni component, making the charge density around the Ni component closer to that of Pt. In addition, the 2D porous structure and heterojunctional interface facilitated the contact of catalytic sites and reactants, as well as mass transfer and diffusion.

2D porous Mo-Ni based heterojunction sheets have been successfully constructed and exhibited excellent catalytic hydrogenation activity toward aromatic nitro-compounds. The catalysts were obtained by the first synthesis of Mo-modified $Ni(OH)_2$ nanosheets followed by heating in air and NH_3 atmosphere. The abundant pore structure and heterogeneous interface of the 2D porous sheets are favorable for mass transfer and provide more active sites. The resultant 2D porous Ni-Ni_3N-NiMoN heterojunction catalysts exhibited excellent catalytic activity for the reduction of the various aromatic nitro-compounds with good maintenance of high catalytic efficiencies even after 10 cycles of reuse. The magnetism of as-prepared 2D Ni-Ni_3N-NiMoN heterojunction catalysts was expected to allow easy separation from the reaction media. This work provides an indicative for designing efficient catalysts by combination of the early and late transition metals.

Declaration of competing interest

The authors declare that they have no known competing financial interests or personal relationships that could have appeared to influence the work reported in this paper.

Acknowledgments

We gratefully acknowledge the support of this research by the National Natural Science Foundation of China (No. 91961111), the Natural Science Foundation of Heilongjiang Province (No. ZD2021B003) and Fundamental Research Funds for the Central Universities (No. 2572022BU05).

Supplementary materials

Supplementary material associated with this article can be found, in the online version, at doi:10.1016/j.cclet.2022.108128.

References

[1] P. Zhao, X. Feng, D. Huang, G. Yang, D. Astruc, Coord. Chem. Rev. 287 (2015) 114–136.
[2] I.C. Gerber, P. Serp, Chem. Rev. 120 (2020) 1250–1349.
[3] J. Strachan, C. Barnett, A.F. Masters, T. Maschmeyer, ACS Catal. 10 (2020) 5516–5521.
[4] K. Murugesan, T. Senthamarai, V.G. Chandrashekhar, et al., Chem. Soc. Rev. 49 (2020) 6273–6328.
[5] N. Garg, A. Sarkar, B. Sundararaju, Coordin. Chem. Rev. 433 (2021) 213728.
[6] X. Tan, J. Qin, Y. Li, et al., Chin. Chem. Lett. 32 (2021) 1451–1455.
[7] S. Chen, L.L. Ling, S.F. Jiang, H. Jiang, Green Chem. 22 (2022) 5730–5741.
[8] C. Jin, Y. Gu, Z. Li, et al., Mater. Chem. Front. 5 (2021) 2798–2809.
[9] M. Zhang, A. Cao, H. Zhang, C. Yang, J. Colloid Interf. Sci. 623 (2022) 63–76.
[10] M. Zhu, L. Zhang, S. Liu, et al., Chin. Chem. Lett. 31 (2020) 1961–1965.
[11] J.J. Yin, F.K. Zhan, T.F. Jiao, et al., Chin. Chem. Lett. 31 (2020) 992–995.
[12] F. Mo, D. Qiu, L. Zhang, J. Wang, Chem. Rev. 121 (2021) 5741–5829.
[13] M. Cortes-Clerget, N.R. Lee, B.H. Lipshutz, Nat. Protoc. 14 (2019) 1108–1129.
[14] B. Li, J.G. Ma, P. Cheng, Angew. Chem. Int. Ed. 130 (2018) 6950–6953.
[15] B. Lang, H.K. Yu, Chin. Chem. Lett. 28 (2017) 417–421.
[16] M. Mon, R. Bruno, E. Tiburcio, et al., J. Am. Chem. Soc. 141 (2019) 13601–13609.
[17] R. Begum, R. Rehan, Z.H. Farooqi, Z. Butt, S. Ashraf, J. Nanopart. Res. 18 (2016) 1–24.
[18] Y.H. Wang, Q. Li, W. Shi, P. Cheng, Chin. Chem. Lett. 31 (2020) 1768–1772.
[19] Q.Q. Li, P. Shen, Y. Tian, X.C. Li, K. Chu, J. Colloid Interf. Sci. 606 (2022) 204–212.
[20] L. Zhang, M. Zhou, A. Wang, T. Zhang, Chem. Rev. 120 (2019) 683–733.
[21] R. Antonangelo, N. Hawkins, M. Carta, Curr. Opin. Electrochem. 29 (2021) 100766.
[22] R. Cai, P.R. Ellis, J. Yin, et al., Small 14 (2018) 1703734.
[23] Y. Luo, S. Fan, W. Yu, et al., Adv. Mater. 30 (2018) 1704576.
[24] D. Formenti, F. Ferretti, F.K. Scharnagl, M. Beller, Chem. Rev. 119 (2018) 2611–2680.
[25] S. De, J. Zhang, R. Luque, N. Yan, Energy Environ. Sci. 9 (2016) 3314–3347.
[26] H. Yan, C. Tian, L. Wang, et al., Angew. Chem. Int. Ed. 127 (2015) 6423–6427.
[27] H.J. Yan, Y. Xie, Y.Q. Jiao, et al., Adv. Mater. 30 (2018) 1704156.
[28] Z. Wang, L. Gu, L. Song, H. Wang, R. Yu, Mater. Chem. Front. 2 (2018) 1024–1030.
[29] D. Karapinar, C.E. Creissen, J.G. Rivera de la Cruz, M.W. Schreiber, M. Fontecave, ACS Energy Lett. 6 (2021) 694–706.
[30] L. Sun, Y. Wang, C. Wang, et al., Chem 7 (2021) 1557–1568.
[31] Y.J. Luo, Q.Q. Li, Y. Tian, Y.P. Liu, K. Chu, J. Mater. Chem. A 10 (2022) 1742–1749.
[32] Q. Liu, L.S. Xie, J. Liang, et al., Small 18 (2022) 2106961.
[33] G. Yang, Y. Jiao, H. Yan, et al., Adv. Mater. 32 (2020) 2000455.
[34] Y. Gu, A.P. Wu, Y.Q. Jiao, et al., Angew. Chem. Int. Ed. 60 (2021) 6673–6681.
[35] K. Cheng, L.I. Wal, H. Yoshida, et al., Angew. Chem. Int. Ed. 59 (2020) 3592–3600.
[36] Y. Duan, Z. Yu, L. Yang, et al., Nat. Commun. 11 (2020) 4798.
[37] D. Wang, X. Kang, Y. Gu, et al., ACS Catal. 10 (2020) 10449–10458.
[38] F. Yang, N.J. Libretto, M.R. Komarneni, et al., ACS Catal. 9 (2019) 7791–7800.
[39] S.J. Li, X. Kang, B.R. Wulan, et al., Small Methods 2 (2018) 1800250.
[40] K. Ge, S. Sun, Y. Zhao, et al., Angew. Chem. Int. Ed. 60 (2021) 12097–12102.
[41] J. Liang, Q. Liu, A.A. Alshehri, X.P. Sun, Nano Res. Energy 1 (2022) 9120010.
[42] T. Sun, X. Zhao, B. Li, et al., Adv. Funct. Mater. 31 (2021) 2101285.
[43] Y.Y. Chen, Y. Zhang, X. Zhang, et al., Adv. Mater. 29 (2017) 1703311.
[44] L. He, W. Zhang, Q. Mo, et al., Angew. Chem. Int. Ed. 132 (2020) 3572–3576.
[45] Y. Ma, T. Yang, H. Zou, et al., Adv. Mater. 32 (2020) 2002177.
[46] M. Ramadoss, Y. Chen, Y. Hu, et al., J. Power Sources 451 (2020) 227753.
[47] Z. Liu, Z. Lu, M. Bosman, et al., Small 14 (2018) 1803233.
[48] Z. Yan, L. Fu, X. Zuo, H. Yang, Appl. Catal. B 226 (2018) 23–30.
[49] Z.R. Li, J. Liang, Q. Liu, et al., Mater. Today Phys. 23 (2022) 100619.
[50] F.F. Ni, Y.Y. Ma, J.L. Chen, W. Luo, J.P. Yang, Chin. Chem. Lett. 32 (2021) 2073–2078.
[51] Y. Wang, J. Mao, X. Meng, et al., Chem. Rev. 119 (2018) 1806–1854.
[52] S. Wang, L. Luo, Z. Li, et al., J. Hazard. Mater. 430 (2022) 128501.
[53] X. Xu, L. Hu, Z.R. Li, et al., Sustain. Energy Fuels. 6 (2022) 4130–4136.
[54] X. Pan, X. Gao, X. Chen, et al., ACS Catal. 7 (2017) 6991–6998.
[55] Q. Wang, J. Shao, J. Xu, et al., J. Colloid Interface Sci. 607 (2022) 253–268.
[56] S.K. Das, M.M.R. Khan, A.K. Guha, N. Naskar, Green Chem. 15 (2013) 2548–2557.
[57] S. Bolisetty, M. Arcari, J. Adamcik, R. Mezzenga, Langmuir 31 (2015) 13867–13873.
[58] F. Yang, C. Chi, C. Wang, Y. Wang, Y. Li, Green Chem. 18 (2016) 4254–4262.
[59] K. Layek, M.L. Kantam, M. Shirai, et al., Green Chem. 14 (2012) 3164–3174.
[60] X. Liu, D. Xu, Q. Wang, L. Zhang, Small 14 (2018) 1803188.
[61] D. Bykov, F. Neese, Inorg. Chem. 54 (2016) 9303–9316.
[62] A.J. Komor, B.S. Rivard, R. Fan, et al., J. Am. Chem. Soc. 138 (2016) 7411–7421.
[63] J. Feng, S. Handa, F. Gallou, B.H. Lipshutz, Angew. Chem. Int. Ed. 128 (2016) 9125–9129.
[64] W.J. Liu, K. Tian, H. Jiang, H.Q. Yu, Green Chem. 16 (2014) 4198–4205.